Nonlinear Trackers Using Image-Dependent Gains

D.D. Sworder, J.E. Boyd, G.A. Clapp, and R. Vojak

Abstract

A maneuvering target is difficult to follow because its turns are hard to identify from noisy position measurements. It is shown here that, even at close range, an image-enhanced architecture is effective in a tracking application. The performance of a nonlinear, dual-sensor algorithm is contrasted with sophisticated radar-only algorithms, and it is shown that sensor utilization can be expanded significantly with a dual-sensor estimation approach.

Introduction

In a low signal-to-noise environment, a maneuvering target is hard to track. In a typical implementation, a sequence of radar measurements is processed to yield an estimate of current position and velocity (filtering). This estimate of target state is extrapolated to the next observation time (prediction), and the sensor line-of-sight is centered at the anticipated location. As long as the target remains within the field-of-view of the sensor, this process continues. Unfortunately, the timing, the sense, and the magnitude of target turns are hard to identify from range-bearing measurements. A bad state estimate (particularly in velocity) will place the sensor ineptly, and the target will not be detected at the next observation time — it will be lost. Loss-of-lock (LOL) obviously has untoward consequences if the tracker is part of a defense system.

In systems with a phased array radar, there is a strong motivation to extend the interdwell (intermeasurement) interval subject to reasonable constraints on LOL. Signal processing at high, fixed sample rates is burdensome, and, with an agile beam radar, extending the interdwell interval permits tracking several targets simultaneously. This desire to reduce sample rate has led to a diverse collection of tracking algorithms. Some are *ad hoc* and are tailored to sharply delimited environments, but others are flexible enough to accommodate a wide range of conditions. The latter often make use of explicit analytical models of the target and maneuver dynamics and the sensor errors. Such algorithms are called model-based and are typified by the (extended) Kalman filter (EKF) and its lineal variants. Model-based trackers use an implicit quantification of the likelihood of various motion paths to balance the exigencies imposed by the need to simultaneously attenuate the wideband observation noise, and respond quickly when the motion mode changes. Unfortunately, with fixed-gain trackers, this must be done by selecting the filter/predictor time constants in some intermediate range. The performance may not be adequate in high tempo encounters; the possibility of LOL during a maneuver dictates high filter gains, and high gains preclude the data averaging desirable during quiescent intervals. Indeed, EKFs without a range-rate measurement are particularly maladroit at estimating the velocity of an agile target and are unable to make accurate projections across interdwell intervals (Sworder *et al.*, 1993a). To overcome their inherent deficiencies, the EKFs must be implemented at high sample rates.

Fundamental issues in tracking are illustrated in the problem of devising an algorithm for following an agile target moving at nearly constant speed in the plane. Maneuvers create multiple motion modes. The different parts of the target path have distinguishing dynamics; e.g., coast without turning is different from a turn left at rate ψ_t radian/s. A deceptively simple model of the planar translational dynamics of a maneuvering vehicle is given by

$$d\begin{pmatrix} X \\ Y \\ V_x \\ V_y \end{pmatrix} = \begin{bmatrix} 0 & 0 & 1 & 0 \\ 0 & 0 & 0 & 1 \\ 0 & 0 & 0 & -\psi \\ 0 & 0 & \psi & 0 \end{bmatrix} \begin{pmatrix} X \\ Y \\ V_x \\ V_y \end{pmatrix} dt + \begin{bmatrix} 0 & 0 \\ 0 & 0 \\ 1 & 0 \\ 0 & 1 \end{bmatrix} d\begin{pmatrix} w_x \\ w_y \end{pmatrix} \quad (1)$$

where the state vector $\mathbf{x}_t$ is composed of (X,Y), the position coordinates, and (V_x,V_y), the associated velocities. The acceleration process consists of two parts: an omnidirectional excitation $\{w_t\}$ and a maneuver turn rate $\{\psi_t\}$. The former can be conveniently represented by a wideband process: let $\{w_x,w_y\}$ be a Brownian motion with intensity W ($dwdw' = Wdt$). The sample functions of the maneuver process are not well described by a "white" noise, nor do they display the smooth paths typical of an orthodox linear-Gauss-Markov (LGM) process (Gwinner, 1992). Rather than being continuous, the turn rate is more closely approximated as piecewise constant, switching between a fixed set of values with the direction of the maneuver acceleration perpendicular to the target velocity; e.g., an oft used model of the maneuver has a state space of size K: $\psi_t \in \{a_i;\ i \in \mathbf{K}\}$ where $\mathbf{K}$ designates the index set $\{1, ..., \mathbf{K}\}$. The motion model (Equation 1) is a hybrid, nonlinear, stochastic differential equation containing both continuous states (positions and velocities) and discrete states (turn rate).

It is difficult to modify LGM models to properly account

D.D. Sworder is with the Department of ECE, University of California, San Diego, La Jolla, CA 92093-0407 (dsworder@ucsd.edu).

J.E. Boyd is with Cubic Defense Systems, San Diego, CA 92186.

G.A. Clapp is with the SPAWAR Systems Center-San Diego, San Diego, CA 92152.

R. Vojak is at 5, rue George Bizet, 91560 Crosne, France.

Photogrammetric Engineering & Remote Sensing, Vol. 65, No. 6, June 1999, pp. 671–678.

0099-1112/99/6506–671$3.00/0

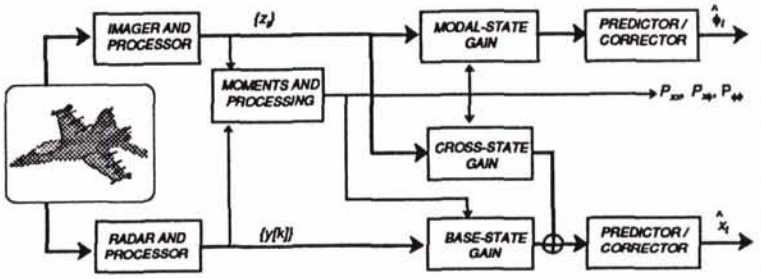

Figure 1. Image-enhanced estimation architecture.

for maneuvers. Proposals for doing this have included treating the maneuver as additive, and affixing an online maneuver detection-and-estimation term to the EKF (Mook and Shyu, 1992); and employing multiple models, in which the effect of the different maneuver modes is represented by different intensities for the omnidirectional acceleration. The former is difficult to implement successfully because the maneuver may change before it has been "identified," leaving the tracker following a phantom motion. The latter suffers from the fact that the sample functions of the maneuver acceleration are far from being white processes. Using either approach, it is exceedingly difficult to incorporate the geometric attributes of the maneuver motion into the filter. Because of the failure to model the maneuver acceleration properly, the correlation between estimation errors in the translational and the rotational states is not used to improve path-following performance.

Despite their limitations, when the tracker depends exclusively on radar measurements, the aforementioned approaches are the best of those currently available. However, as the use of electro-optical (EO) imagers has become accepted, new tracking architectures are possible. The dual-path configuration shown in Figure 1 has been proposed for this application (Sworder *et al.*, 1993b). The radar provides a center-of-reflection measurement of the target, i.e., range and bearing along the line-of-sight to a point-equivalent object. An imager uses visual, infrared, or second-order radar products to infer relevant spatial attributes of the target, specifically, the target orientation with respect to the line-of-sight of the imager (Kuhl, 1992). The observation sequence from the radar will be designated $\{y_t\}$ (or $\{y_k\}$ if reference is made to the radar measurement at the k-th dwell taken with an interdwell interval of T seconds. This range-bearing measurement can be modeled (with suitable linearization, see Maybeck (1982)) as $y_t = Dx_t + n_t$ at observation times, where $\{x_t\}$ is the location state and $\{n_t\}$ is a "white" measurement noise with covariance $\mathbf{R}_x > 0$. The radar "gain," D, depends upon the target-sensor geometry and will vary during an engagement.

Target orientation is measured with an EO-imager every T' seconds (or at a rate $\lambda = 1/T'$ frames/second) yielding a measurement sequence $\{z_t\}$ (or $\{z_k\}$ if the frame number is to be emphasized). The form that this measurement takes depends upon the sensor; e.g., z_t could be the true orientation observed in a noisy channel (Andrisani and Kuhl, 1992; Table 8). This paper uses a measurement framework that differs fundamentally from that of the EKF. The orientation sensor is an image classifier which places the measured orientation into one of L equally spaced orientation bins: $\{z_t\}$ is an L-dimensional counting process, the i-th component of which is the number of times on $[0, t]$ the imager has placed the target orientation in bin i. The quality of the imager is determined both by the frame rate, λ, and by the fidelity of the processing of a single data frame, the latter embodied in an L by L discernibility matrix $\mathbf{P}$: $\mathbf{P}_{ij}$ is the probability that the target will be classified as being in bin i if j is the true orientation bin. Measured target orientation is used to infer the maneuver state in the upper path of Figure 1.

Let $\{\alpha_t\}$ be the maneuver indicator process; $\alpha_t = \mathbf{e}_i$ if $\psi_t = a_i$.[1] Equation 1 can be written

$$dx_t = \Sigma_i A_i x_i \alpha_i dt + B dw_t \tag{2}$$

where the definition of $\{A_i; i \in \mathbf{K}\}$ is clear from Equation 1. The maneuver tempo will be quantified by supposing that ψ_t is a Markov chain with K by K transition-rate matrix q. The angular bin sequence will also have a Markov representation for a specific turn rate; e.g., if $\alpha_t = \mathbf{e}_m$, then the indictor process of the true angular bin, $\{\rho_t\}$, is Markov with transition rate matrix $\mathbf{Q}^m$. The comprehensive maneuver state of the target is given by $\phi_t = \alpha_t \otimes \rho_t$, and $\{\phi_t\}$ is a Markov process with KL by KL-dimensional transition-rate matrix $\mathbf{Q} = (q \otimes \mathbf{I}_L) + \text{diag}(\mathbf{Q}^i; i \in \mathbf{K})$.

A gain adaptive tracker, the polymorphic estimator (PME), was proposed in Sworder *et al.* (1993c), and effectively fuses the "point" and "extended-body" data sequences. The PME algorithm first uses the image data to estimate the maneuver state (the PME-orientation filter), and this estimate is then used both additively and multiplicatively in the filtering/prediction link. Specifically, define the vector mean observation rate $\boldsymbol{\lambda}_t = \lambda \mathbf{P}(\mathbf{1}_K' \otimes \mathbf{I}_L)\phi_t$, and use a circumflex to denote conditional expectation. The i-th component of $\boldsymbol{\lambda}_t$ is the expected rate of receiving the i-th observation for a given maneuver state; i.e., for a given turn rate×true orientation-pair. Because the measured orientation depends only on true orientation, the factor $(\mathbf{1}_K' \otimes \mathbf{I}_L)$ reduces ϕ_t to ρ_t. The PME algorithm is most concisely written in terms of a modified version of the image measurements. Let $\{\vartheta_t\}$ be a process that is constant between image observations, with increments $\Delta\vartheta_t = \lambda \mathbf{P}' \text{diag}(\hat{\boldsymbol{\lambda}}^{-1}) \Delta z_t$ when an image observation is received. Then, the maneuver estimate is found from the stochastic equation:

$$\text{A. Between observations: } (d/dt)\hat{\phi}_t = \mathbf{Q}'\hat{\phi}_t \tag{3A}$$

$$\text{B. At an observation time: } \hat{\phi}^+ = \text{diag}(\mathbf{1}_K' \otimes \Delta\vartheta)\hat{\phi}^- \tag{3B}$$

subject to an appropriate initial condition.

Estimates of position and velocity are given by the PME-translation filter. This algorithm has a more conventional form, mapping the radar measurements into an estimate of position and velocity, with gains that are functions of both the image and the radar measurements:

[1]Note: $\mathbf{e}_i$ is the i-th canonical unit vector in the vector space appropriate to the context, $\mathbf{I}_K$ is a K-dimensional identity matrix, $\mathbf{1}_K$ is a K-vector of ones, and $\otimes$ indicates Kronecker product.

A. Between observations:

$$(d/dt)\hat{x}_t = \Sigma_i A_i((P_{x\phi})_{.i} + \hat{x}_t\hat{\phi}_i) \quad (4A)$$

B. At a radar measurement:

$$\Delta\hat{x}_t = \mathbf{P}_{xx}\mathbf{D}' (\mathbf{D}\mathbf{P}_{xx}\mathbf{D}'+\mathbf{R}_x)^{-1} \Delta\nu_t \quad (4B)$$

C. At an image measurement: $\Delta\hat{x}_t = \mathbf{P}_{x\phi}(\mathbf{1}_K'\otimes)\Delta\vartheta)$ (4C)

where $\Delta\nu_t = y_t - \mathbf{D}\hat{x}_t$ (the increment in the translational innovations process), and ($\mathbf{P}_{xx}$, $\mathbf{P}_{x\phi}$) are the (random) second central moments of the estimation error. The moments are dependent upon the image measurements and the filtered estimate of the target path. The equations for their calculation are derived in Sworder and Vojak (1994a).

Equation 4 is similar in form to the EKF. If the correlation between x_t and ϕ_t is neglected, Equation 4C disappears, Equation 4A becomes $(d/dt)\hat{x}_t = \hat{A}_t\hat{x}_t$, and Equation 4B becomes the orthodox Kalman update. As written, Equation 4 differs from the EKF because it utilizes the geometry of the motion path in the computation of the joint orientation-translation cross central moment $\mathbf{P}_{x\phi}$. (Note that an analogous moment for a different sensor type is computed as part of the EKF proposed in Andrisani *et al.* (1992)). Further, the translational error covariance, $\mathbf{P}_{xx}$, is contingent upon both the estimated target path and the image sequence. The former dependence occurs in the conventional EKF but the latter is novel. To gain a perspective on the salient differences between the PME and radar-exclusive trackers, certain properties of the PME should be noted. The PME-translation filter uses a single model for extrapolation; i.e., Equation 4A is four-dimensional, with extrapolation dynamics weighted by output of the PME-orientation filter. Equation 4A neither averages the maneuvers, nor treats the maneuver acceleration as additive; it maintains both the separateness of the maneuver classes and the geometry of the maneuver acceleration and the target velocity. The update after a radar measurement, Equation 4B, has a conventional form with the caveat that the multiplier $\mathbf{P}_{xx}$ is responsive to the image sequence. The image update (Equation 4C) sets the PME apart most distinctly from the radar-exclusive algorithms in which it plays no role. The correlations between errors in estimating the translational and rotational states are used directly to update the translational estimate. This direct image-to-translation update is possible only because the relevant second moment, $\mathbf{P}_{x\phi}$, is computed as part of the PME.

The effectiveness of the PME derives from its ability to use the image information both for direct updates, and for adjustments to the tracker gains and time constants. But the image path is justified only through improvement in tracker performance, and not by its accuracy in maneuver classification; if the PME-orientation estimate has a liminal influence on the PME-translation filter, the increased complexity of the image-enhanced architecture would not be warranted. It is difficult to isolate the primary influence of the imager. However, the behavior of the translation error covariance matrix, $\mathbf{P}_{xx}$, gives considerable insight into how image information is used to adapt the tracker to changing motion status. In the radar update equation (Equation 4B), the innovations gain is a function of $\mathbf{P}_{xx}$. Because $\mathbf{R}_x$ is usually fixed, and $\mathbf{D}$ is either constant or varies smoothly on the path, it is through $\mathbf{P}_{xx}$ that the balance between data smoothing and modal adaptation is achieved. When $\mathbf{P}_{xx}$ is large, the increment in the innovations process is valued more highly as regards location updates than when it is small; when the filter is uncertain about the target location, it becomes more data-driven. Trackers which identify turns from radar data must adjust $\mathbf{P}_{xx}$ in an *ad hoc* manner to account for increased uncertainty near changes in motion mode. In the PME, the image data are used to manage this "hand-off" problem.

In what follows, the PME is used in two tracking applications: tracking a cruise missile on approach to a ship, and following a maneuvering ground vehicle. In the former, the missile path moves in all three position coordinates, but in both examples, the active portion of the target path lies in a fixed plane. This restriction permits the planar model given in Equation 1 to be used to describe target motion. In both examples, the location measurement is of a conventional sort: range and bearing. In the first example, a realistic model of a currently deployed phased array radar is used. The radar model includes random data dropouts, sensitivity to angle off of line-of-sight, and highly nongaussian measurement errors. The second example uses an additive Gaussian noise model to represent location measurement errors.

The discernibility matrix, $\mathbf{\Phi}$, parameterizes the quality of the imager/image processor. Practical methods of classifying orientation from a single image frame lead to errors that are not well modeled with additive noise. A useful taxonomy separates the imager error into three categories and constructs $\mathbf{\Phi}$ from these primitives. Because the examples are planar, the image orientation bins are naturally constructed by dividing the circle into bins of width $2\pi/L$ radians; the matrix $\mathbf{\Phi}$ is L by L. The most distinctive image error occurs when the ostensible orientation bin is symmetrically placed about a line perpendicular to the line-of-sight. This error source represents the generic ambiguity which arises when the target orientation classifier relies heavily on a projection of an extended object. It is pointed out in Taylor *et al.* (1992) that, when a target has bilateral symmetry, any image interpretation method which relies exclusively on a two-dimensional projection of the target shape will be interpreted erroneously at least half of the time. The use of internal features, derived from EO or range information, can be used to reduce the probability of projection error. Figure 7 of Taylor *et al.* (1992) shows the sensitivity of image classification to the number of measured features for a target moving in three dimensions. Utilizing additional target features, the probability of correct classification can be increased to the range of 65 percent to 90 percent.

Other sources of image distortion include local image degradation due to pixel noise and quantization, or, more globally, severe occlusion of the image. The former source will be represented by assuming that the image is misclassified symmetrically into a neighboring bin (spillover error). The latter results in errors of large magnitude, and will be represented by assuming that the image is classified with uniform probability across all possible angular bins. This macroerror could be reduced in significance by the "class-type" identification proposed in Taylor *et al.* (1992), but this is not done here. The maneuver model describes the dynamic evolution of orientation, and this permits the use of Equation 3 to partially resolve the symmetry errors described above, in particular, minimizing the influence of the "folded angle" ambiguity discussed in Taylor *et al.* (1992). Andrisani *et al.* (pers. comm., 1996) propose to extend the utilization of a motion model to include the estimates of the kinematic states to aid in image disambiguation. This approach has been shown to reduce the aliasing error to 1 percent in some cases. This sophisticated feedback is not used in the PME where the maneuver state is inferred from the imager measurements alone.

An Example: Cruise Missile Tracking

To illustrate the utility of image-augmentation, a specific scenario will be considered in some detail. An anti-ship missile is launched at a range of 80 km, an altitude of 1 km, and a velocity of 300 m/s. After a free fall to 780 m, the missile approaches the ship at a velocity of 335 m/s. Nearing the ship at constant altitude, the missile performs a series of 7-g jinks, coasts for 10s, and then makes a final 3-g turn toward its in-

tended destination. The constant altitude portion of the path is shown in Figure 2.

The translational observations are generated by a GHz-band, phased array radar using amplitude-comparison monopulse with uniform illumination across the array. The array consists of 3600 individual elements with cosine illumination. The broadside is directed at 0° in bearing and 10° in elevation. The two-way radar beam has a 3-dB beamwidth in the sum channel of 1.2° at the broadside direction. The range gate is 1550 meters with range bins of 50 meters. Investigators at Naval Surface Warfare Center, Dahlgren Division, have created a realistic model of the radar (Blair *et al.*, 1994). Additionally, Blair and his coworkers at the Naval Surface Warfare Center developed an EKF compatible with this particular radar. The Blair-EKF will be used as normative in what follows.

Several independent groups of investigators have devised radar-exclusive trackers for this cruise missile trajectory. The simplest algorithm is an α-β tracker (α is the position gain and β is the velocity gain) with an identification logic to detect maneuvers and change the tracker gains (Rhatigan *et al.*, 1994). Satisfactory performance was obtained from the α-β tracker with an interdwell interval of 0.75s: approximately 2 percent LOL on a small sample. In Sastry *et al.* (1994), a more sophisticated approach was proposed. An auxiliary processor was used to estimate the timing and sequencing of the maneuvers. The influence of the ostensible maneuvers was then included in an EKF-like algorithm. With an interdwell interval of 0.5s, the LOL rate was approximately 1.5 percent. Sample functions of the "identified" maneuvers show good accuracy, but with a delay sufficient to cause the maneuver estimate to lag the true by several seconds (see Figure 1 of Sastry *et al.* (1994)), an important lag when the maneuver durations are themselves on the order of a few seconds. A third approach, the interacting multiple model (IMM) algorithm, has been shown to be highly efficient for radar-based tracking. In Daeipour *et al.* (1994), three models, each with a different white-noise intensity, were used to model coast, a continuing maneuver, and the start-or-end of a maneuver. The IMM with a variable interdwell interval (with mean 1.5s) was shown to yield an LOL rate of 3 percent (as compared with an LOL rate of 54 percent with a similarly designed EKF).

With its additional sensor, the PME is not directly comparable to the algorithms described above. For this study, the PME uses a nominal 3-s radar interdwell interval, accommodating to a failure to receive a return by requesting a new radar sample after 0.1s. A collocated imager/processor measures target orientation. In what follows, it will be supposed that target orientation bins are 10° wide ($L = 36$), and the image frame rate is $\lambda = 1$ image/s; i.e., a target image is created every second, and it is processed and placed into one of 36 bins (image latency will be neglected at this sample rate). The discernibility matrix, $\mathbf{P}$, is constructed from the error primitives: (1) with probability 0.1, the target is placed in the bin symmetric to the true orientation; (2) with probability 0.05, the target is placed in an bin adjacent to the true bin; and (3) with probability *Be*, the target is placed in an arbitrary bin. As pointed out earlier, the first error source represents the generic ambiguity arising from projecting a three-dimensional object into a lower dimension (described as a $2^1/_2$-dimensional projection in Taylor *et al.* (1992)). The second represents spillover errors from the images near a bin boundary. The third represents the output of the image classifier when the image is so contaminated that the categorization of the image is arbitrary. The probability of capricious classification, *Be*, is a parameter in this section.

The radar interval used by the PME is selected to be approximately twice that used with the most sophisticated of the radar-exclusive algorithms (and four times the less sophisticated), and the image frame rate is relatively slow and is comparable with the scan rate of current IRST implementations. In what follows, tracking on the subinterval [120, 140]s will be explored (see exploded frame in Figure 2). This has a short coast (2s), a hard left (10s), a brief coast (3s), and a hard right (5s). A simplified maneuver state space is used to represent the scenario: $\Psi_t \in \{a_{1,2} = \pm 0.2$ r/s, $a_3 = 0$ r/s$\}$. The PME must resolve the motion modes from image frames that are few in number (one per second), and contaminated with noise. Note that the subpath is more difficult to follow than the full path would be because the tracker has no opportunity to initialize itself on the long initial coast; the normative EKF lost lock on *every* trial of this subpath even when using the radar at a sample rate of 20 samples/s. This shortened scenario provides a stiff test for the tracker, and it illustrates the implications of a failure to identify the presence of a target until it is close to its objective.

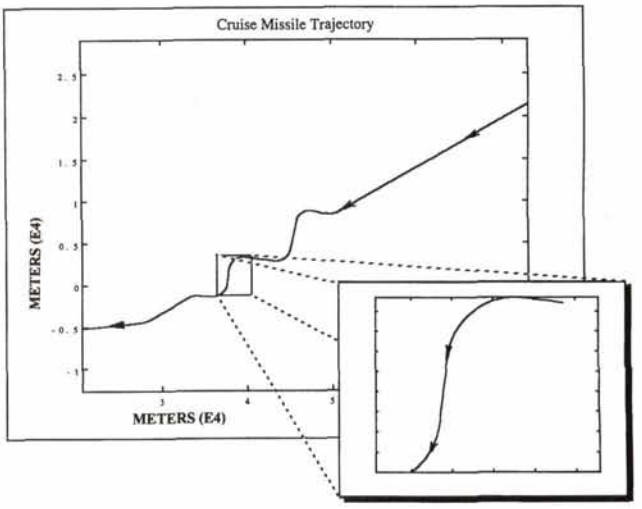

Figure 2. Path of an anti-ship missile.

The performance of an image-enhanced tracker is sensitive to image quality; as image quality degrades with range, clutter, processing elegance, etc., LOL tends to increase. In this scenario, the image sample rate is such that few data frames are taken during each of the maneuver modes. If an image is too contaminated to classify properly, the PME must extrapolate across multiples of the interframe time. Figure 3 shows the variation of LOL as a function of *Be*. The LOL rates are deduced from a simulation of the trajectory and the radar-imager, using a sample of size 30 for each *Be* tested — and are shown as the small circles in the figure. When *Be* is small ($Be < 0.25$), the PME almost never lost lock — once in 150 trials. By the time *Be* moves beyond 0.4, the LOL rate increases to an unacceptable level (approximately 10 percent at $Be = 0.4$). Observe that, with a *Be* of 0.4, image classification is correct less than half the time; on the 2-s coast used for initialization, the PME expects only one good piece of data.

Each element in the error taxonomy has an idiosyncratic (and synergetic) influence on LOL. Hence, $\mathbf{P}$ is not well described by a single number, e.g., standard deviation of the image error. It is nevertheless interesting to compare the performance of the PME with other algorithms. Andrisani *et al.* (1992; Figure 2) present a parametric study of imager effectiveness on a slower speed, coast-turn path with interdwell intervals for both the radar and the imager of 0.1s. Both types of measurement were taken in additive white-noise channels. For these sensors, it was shown that image enhance-

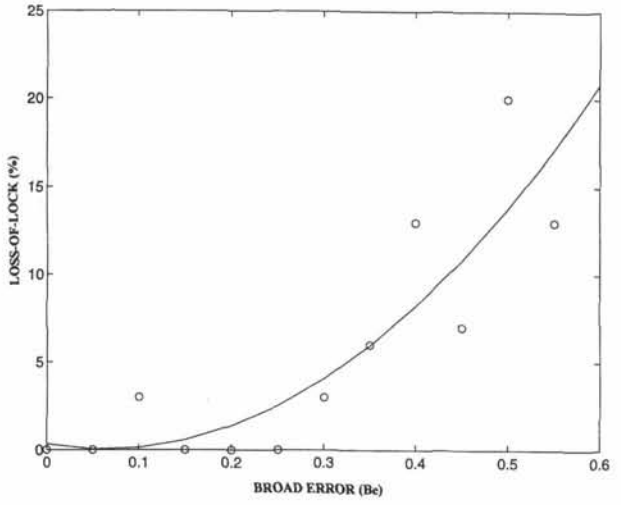

Figure 3. Probability of loss-of-lock as a function of *Be*.

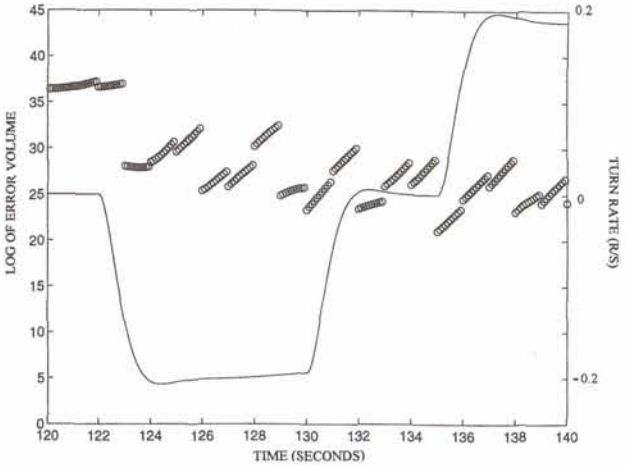

Figure 4. The log of the $\mathbf{P}_{xx}$ error volume and the turn rate along the sample path: $Be = 0.1$.

ment leads to significantly improved tracking performance when the standard deviation of the orientation measurement error is in the range 2 to 7 degrees. By way of comparison, the PME with $Be = 0.4$ has a standard deviation in the angular measurement of approximately 66° due to *Be* alone. The effect of the other errors depends upon target orientation, but the total angular standard deviation exceeds 70°. Even with this imprecision, the PME maintains lock on this near-range scenario under conditions that cause the normative EKF to fail even with a 60-to-1 advantage in radar sample rate.

The PME utilizes the image measurements to adapt its gains to the maneuver mode. Even with a high fidelity imager, the slow sample rate precludes resolution of the maneuver status with high confidence. The maneuver dynamics interact with classification errors to cause the PME-orientation algorithm to maintain a conservative demeanor. The PME responds more quickly to maneuvers than does the detection/identification algorithm proposed in Sastry *et al.* (1994), but, without the postprocessing of the latter algorithm, the precise shape of the maneuver is never clearly delineated. The advantage of the image-enhanced algorithm lies not in its ability to recreate the sample path of the turn rate, but instead, in its ability to maintain the proper geometric relationship between the maneuver acceleration and the velocity.

Loss-of-lock rate is the central measure of tracking performance, but this single number masks the detailed behavior of the system. Figure 4 shows a sample function of the log of the product of the eigenvalues of $\mathbf{P}_{xx}$ along the path (shown as the small circles and using the left scale) and the actual turn rate (shown as the continuous curve and using the right scale). The Markov model for the turn rate process is seen to be only a coarse approximation to its realization, but effective nonetheless as indicated by the infrequent target losses. The log of the product of the eigenvalues of $\mathbf{P}_{xx}$ (a positive symmetric matrix) gives an indication of the error volume in the location × velocity state space as computed by the PME. After a three-second initialization, $\{\log \Pi_{i=1,\ldots,4} \lambda_i(\mathbf{P}_{xx})\}$ falls into a pattern of significant decrease after every radar measurement (at 123s, 126s,....), and smaller changes (of both signs) at the image updates (e.g., at 127s, 128s, 131s). The reduction in the error covariance after a radar update is an oft noted characteristic of the Kalman filter, but the image-induced changes are novel. Analysis of other tracking data (not presented here) suggests that the largest image-coincident changes occur when there are significant changes uncertainty in maneuver detection; i.e., changes in $\Sigma_\ell \hat{\phi}_\ell(1 - \hat{\phi}_\ell)$ resulting from an image observation that the PME found persuasive. When the PME-orientation filter is less sure of the maneuver mode, it causes the PME-translation filter to reduce its time constants, and conversely. The error volumes are seen to be relatively insensitive to the motion mode, with an initialization transient that takes several measurement cycles.

Another measure of filter performance is prediction error, the magnitude of the difference between the predicted and true target position. Prediction error tends to grow between measurements, and it is sensitive to changes in the motion mode — LOL ends to occur after a sudden turn. Even if lock is maintained, it is important to have a sense of the size and distribution of prediction error; e.g., for fire control calculations. Figure 5 shows two snapshots of prediction error, both computed on a sample of size 50, with the filter initialized to the true state at time 113s to eliminate the effect of effect of the initialization transient. The first snapshot shows the error likelihood at $t = 124.9$s, a full second into the first left turn. The extrapolation error is concentrated near zero with a few significant outliers. Also plotted is a Rayleigh density with the same mean as that of the prediction error. If the errors in the X and Y direction were independent zero-mean Gaussian random variables with the same variance, the prediction error would be Rayleigh. It is seen that the error in strongly nonGaussian, thus explaining in part the poor performance of the normative EKF.

The second snapshot it taken at $t = 139.0$s, the most demanding point on the path. The target has ended its first turn, coasted for only 3s, and begun a turn in the other direction. The mean of the sample error is somewhat larger than it was at $t = 124.9$, but the sample distribution is more concentrated near the mode; the error does not have zero mean, but it is biased primarily because of the lag in responding to the new turn. Again, it is evident that the Gaussian hypotheses underlying the EKF will lead to grief when applied here.

Renewal Models

Parasitic effects make the sojourn times in an angular bin random even when the nominal turn rate is known. Further, the finite state space for acceleration is an abstraction used to describe what is actually a continuum of possible actualizations (see Figure 4). For example, a_1 is but a single element in an interval (bin) of rotation rates; a_1 is close to, but likely

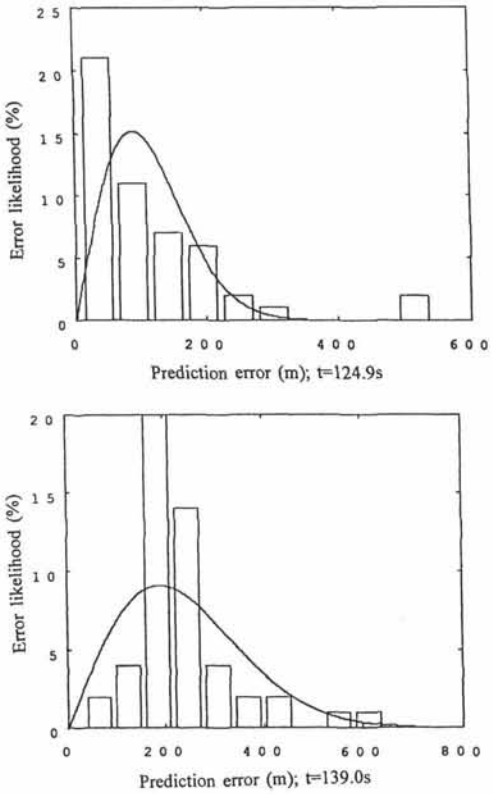

Figure 5. Histogram of prediction error at times t = 124.9s and 139.0s.

not identical to, the actual value of Ψ_t even when Ψ_t is in the a_1 bin. In the basic PME, the orientation bin sequence is assumed to be a Markov process for a specific turn rate. Suppose $\Psi_t = a_m$ for an a_m in the direction of increasing bin number. The Markov model presents target orientation as remaining in an angular bin with an exponentially distributed residence time (mean $2\pi/La_m$), after which the bin indicator process, $\{\rho_t\}$, transitions $\mathbf{e}_k \rightarrow \mathbf{e}_{k+1}$; the faster the turn, and/or the smaller the bin, the shorter the mean time within the bin, with the direction fixed by the sense of the turn. This representation for bin sojourns has an obvious weakness: exponential distributions have an excess of very short and very long lifetimes. While the Markov bin model has proven to be serviceable, it does not manifest the quasi-periodicity underlying the angular motion well; e.g., if the frame rate is high, the orientation is unlikely to enter a bin at one frame time and exit it the next, but the exponential model masks this trait.

It is possible to create a more realistic sojourn model for target orientation by using a gamma density. A γ-density is a two parameter family, $\gamma(t;R,\Lambda)$, in which R controls shape and Λ controls time scale: $\gamma(t;R,\Lambda) = I_{[t>0]}\, \Lambda(\Gamma(R))^{-1}(\Lambda t)^{R-1}\exp(-\Lambda t)$; $R,\Lambda>0$. The mean of a gamma distributed random variable is $\nu = R/\Lambda$, and ν will be used to indicate the time scale. Figure 6 shows three γ-densities, and it is evident that, as R increases, the transition events become more regular. To adjust the PME for this, more realistic, orientation model, first fix the turn rate; e.g., $\alpha_t = \mathbf{e}_m$. Select a γ-density (with parameters (ν_m, R), the latter integer valued) that best describes the sojourn times associated with an angular bin residence for the given acceleration. R could depend upon the turn rate (i.e., m) too, but the changes that result from this generalization are transparent. Partition the sequence of integers

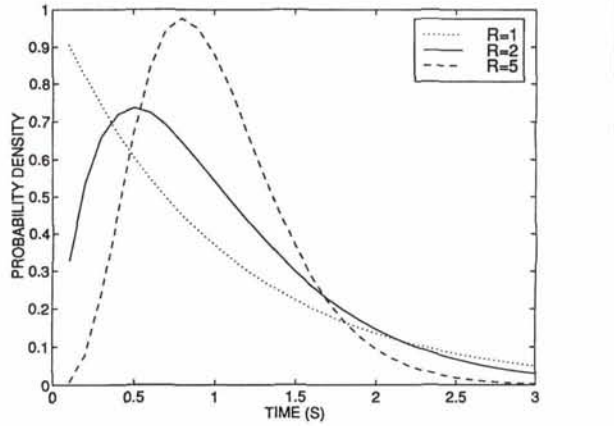

Figure 6. Gamma distributions for R = 1, 2, and 5; mean equal 1.0 seconds.

RL into L, equally spaced contiguous blocks: $\mathbf{A} = \mathbf{A}(1) \cup ... \cup \mathbf{A}(L)$; $\mathbf{A}(1) = \{1,...,R\}$, $\mathbf{A}(2) = \{R+1,...,2R\}$, and so on. The orientation model replaces each substantive angular bin with R subbins; i.e., as the orientation moves across a single **true** bin (the k-th say), the model has it traverse R **ersatz** bins (labeled $\mathbf{A}(k)$). Let r_t be an R-dimensional indicator. In this new framework, the orientation is given by the unit vector $\rho_t \otimes r_t$, the former denoting the true angular bin, and the latter, the sub-bin. To preserve the mean time angular change of the target, the mean time in each of the sub-bins must be reduced by the factor R ($\nu_m = 2\pi/RLa_m$). The joint (acceleration $\times$ orientation) process is now Markov even for the γ-renewal residence times, albeit in a state space of higher dimension: the maneuver state of the target is $\phi_t = \alpha_t \otimes \rho_t \otimes r_t$. The transition rate matrix for the orientation model associated with the m-th maneuver mode can be deduced in a direct manner.

To illustrate the performance of the modified PME, consider a slower paced coast-turn-coast path of a tank or APC. The target is initially located at (X_0, Y_0) = (1.0, 6.4) km, and moving at constant velocity (V_{x0}, V_{y0}) = (5.0, −13.3) m/s for $t \in [0, 10)$s. A 0.3-r/s turn is made during $t \in [10, 20)$s, after which the target returns to constant velocity motion. Figure 7 shows the target path (labeled truth) without the wide band

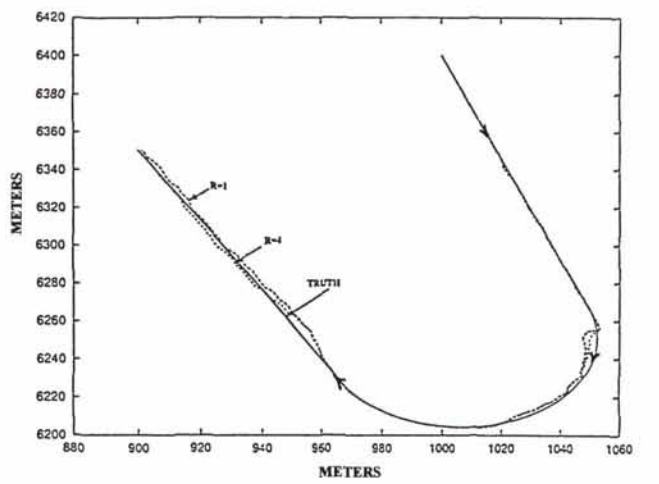

Figure 7. Mean tracking performance for two values of R.

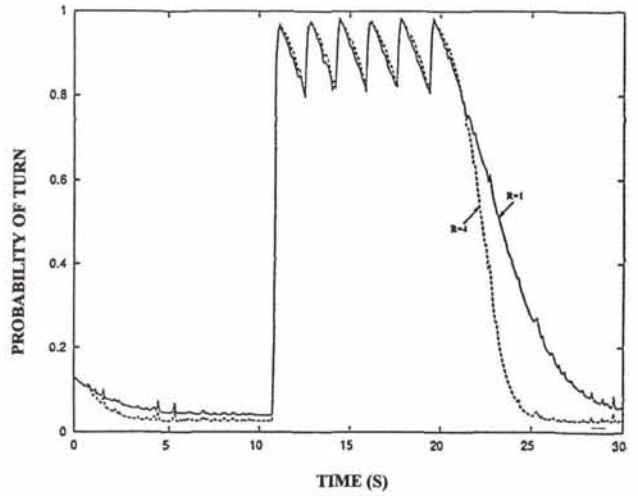

Figure 8. Probability of coast as determined from the image information.

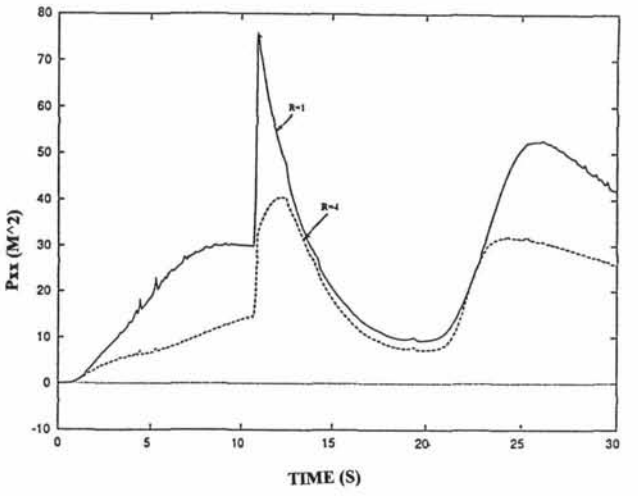

Figure 9. The value of $\mathbf{P}_{xx}$ along the path for two values of R.

acceleration. Tracking will be accomplished with two sensors: a conventional range-bearing sensor located at (0, 0) and a collocated imager. The sensors take measurements simultaneously every 0.1 seconds. Sensor qualities are as follows: the position sensor measures true location in additive Gaussian noise with a standard deviation 5.0 meters in range and 0.25° in bearing; the orientation sensor partitions the angular field into 30° bins ($L = 12$), and the discernibility matrix, $\mathbf{\Phi}$, is constructed from the following error primitives, (a) with probability 0.29, the target is placed in the bin symmetric to the true orientation; (b) with probability 0.03, the target is placed in a bin adjacent to the true bin; and (c) with probability 0.01, the target is placed in an arbitrary bin. The imager misclassifies its observation a third of the time. The omnidirectional accelerations will be assumed to be slight: $W = 0.01\mathbf{I}$ $(m/s^2)^2$. The maneuver state space will be three dimensional; $\{a_1 =$ coast, $a_{2,3} = \pm 0.3$ r/s$\}$, with the chain $\{\alpha_t\}$ symmetric about the coasting mode and coasting always interjected between turns (no jinking). Specifically, the following tempo is assumed: $\nu_1 = 20$s; $\nu_{2,3} = 10$s.

Figure 7 shows the response of two PME-trackers in the $\{\alpha_t; \mathbf{e}_1 \rightarrow \mathbf{e}_3 \rightarrow \mathbf{e}_1\}$ *scenario*: PME($R = 1$) (Markov PME) and PME($R = 4$) (quasiperiodic bin crossings). To display biases, 20-trial mean sample paths are shown rather than the (noisier) single sample paths. Both of the trackers perform well in the premaneuver phase, but deviate slightly during and after a turn. Their performance is far superior to the conventional EKF (Sworder and Vojak, 1994b). The corresponding velocity profiles (not shown) display similar behavior, and are again far superior to the orthodox EKF.

The nonMarkov bin-sojourn model portrays more accurately the bin dynamics than does the Markov model. Figure 8 shows the sample average of the conditional probability of "turn right." Note that both algorithms are delayed in recognizing the beginning of a turn (it starts at $t = 10$s); the orientation must pass a bin boundary before a turn is manifest in the angular data. Despite the improved model, the nonMarkov algorithm is little better than is its Markov counterpart during the turn. The return to coast is much more expeditiously determined in the PME($R = 4$)-orientation filter though. Both models "decay" to coast, but the rate of the nonMarkov algorithm is much faster. This improvement in rotation estimation is not, however, reflected in a substantive improvement in track error.

Although tracking performance (as contrasted with maneuver identification) is little different in the two algorithms, PME($R = 4$) achieves its goals with generally lower gains. Figure 9 shows the sample average of the computed conditional X-covariance (see Equation 4B). Both algorithms adjust their gain as the path uncertainty changes; high gains during times of higher uncertainty and conversely. But PME($R = 4$) generates moments that are generally smaller, and in some cases much smaller than its Markov counterpart. The $R = 4$ algorithm has the desirable property that is able to track well, but with smaller gains (and consequently less magnification of the observation noise). It is, however, more complex to implement.

Conclusions

This paper presents a study of performance improvements possible with image enhancement. Using a simulated phased-array radar, it is shown that a target of the cruise missile class can be followed with low probability of LOL and with an interdwell interval that is nominally 3s. This compares favorably with the most sophisticated of the radar-exclusive algorithms. An improvement by a factor of almost two is achieved with an imager whose ability to discern a turn is not particularly good. The advantage of proper modeling of the nonlinear engagement dynamics and utilizing the extended set of cross moments is evident.

The sample rate of the imager is rather slow for the cruise missile scenario. In general, the imager frame rate can be reduced only if the processing fidelity is increased. In the fleet defense example, the short sojourns in each of the motion modes precludes extending the interframe intervals of the imager much more. Tests indicate, however, that the benign portions of the path, e.g., the initial coast at long range, can be handled quite well with a lower frame rate.

This paper also suggests, by means of an example, that the performance improvement attainable from using a more accurate model of target rotation (a nonMarkov renewal model) may not be worth the additional effort to implement it. The Markov PME performs well even when a rudimentary model is used. This tracker appears to be sufficiently robust as to not need the additional computation that a high accuracy maneuver model entails. However, a lower gain implementation is possible if the nonMarkov representation is used.

References

Andrisani, D., and F.P. Kuhl, 1992. Attitude Based Trackers for Airplane, Helicopter and Ground Targets, *Remote Sensing Reviews*, 6:11–31.

Andrisani, D., E.T. Kim, and F.P. Kuhl, 1992. Tracking Accuracy Improvement Using Noisy Target Orientation Measurements, *Remote Sensing Reviews*, 6:49–63.

Blair, W.D., G.A. Watson, and S.A. Hoffman, 1994. Benchmark Problem for Beam Pointing Control of Phased Array Radar Against Maneuvering Targets, *Proc. of the 1994 American Control Conf.*, pp. 2071–2075.

Daeipour, E., Y. Bar-Shalom, and X. Li, 1994. Adaptive Beam Pointing Control of a Phased Array Radar Using an IMM Estimator, *Proc. of the 1994 American Control Conf.*, pp. 2093–2097.

Gwinner, H.G., 1992. The Maneuvering Target, *Maneuvering Targets and Gun Fire Control Technology* (H.H. Burke, editor), GACIAC SOAR 92-01, ITT-Research Institute, Chicago, Illinois, pp. 1–58.

Kuhl, F.P, 1992. Radar Recognition of Geometric Classes in Free Space, *Remote Sensing Reviews*, 6:331–349.

Maybeck, P.S., 1982. *Stochastic Models, Estimation, and Control, Vol. 2*, Academic Press, New York.

Mook, D.J., and I-M Shyu, 1992. Nonlinear Aircraft Tracking Filter Utilizing Control Variable Estimation, *Journal of Guidance, Control and Dynamics*, 15:228–237.

Rhatigan, B.T., P.R. Kalata, and T.A. Chmielewski, 1994. An α-β Target Tracking Approach for the Benchmark Tracking Problem, *Proc. of the 1994 American Control Conf.*, pp. 2076–2080.

Sastry, C.R., B.J. Slocumb, P.D. West, E.W. Kamen, and H.L. Stalford, 1994. Tracking a Maneuvering Target Using Jump Filters, *Proc. of the 1994 American Control Conf.*, pp. 2081–2087.

Sworder, D.D., R.G. Hutchins, and M. Kent, 1993a. The Utility of Imaging Sensors in Tracking Systems, *Automatica*, 29:445–449.

Sworder, D.D., P.F. Singer, D. Doria, and R.G. Hutchins, 1993b. Image Enhanced Estimation Methods, *IEEE Proceedings*, 81:797–812.

Sworder, D.D., R. Vojak, and R.G. Hutchins, 1993c. Gain Adaptive Tracking, *Journal of Guidance, Control and Dynamics*, 16:865–873.

Sworder, D.D., and R. Vojak, 1994a. Hybrid Estimation Algorithms, *Journal of Optimization Theory and Applications*, 81:143–167.

———, 1994b. Tracking Mobile Vehicles Using a NonMarkovian Maneuver Model, *Journal of Guidance, Control and Dynamics*, 17: 870–872.

Taylor, R.W., A.P. Reeves, and F.P. Kuhl, 1992. Method for Identifying Object Class, Type and Orientation, in the Presence of Uncertainty, *Remote Sensing Reviews*, 6:183–206.

(Received 24 March 1997; revised and accepted 31 July 1998; revised 04 September 1998)

Instituto Panamericano de Geografía e Historia (IPGH) Comisión de Cartografía Reunión Técnica

La Comisión de Cartografía del IPGH ha programado una reunión técnica en la Universidad de Panamá, del 22 al 26 de setiembre de 1999, con el fin de discutir problemas técnicos que enfrentan países de Centro y Sudamérica en las áreas de Cartografía, Sensores Remotos y Sistemas de Información Geográfica e Información Geoespacial.

El objetivo de esta reunión, que cuenta con la participación de los representantes del IPGH de Centro y Sudamérica, es el de identificar proyectos técnicos que toquen temas de importancia en estas áreas. Para el IPGH y otros organismos no-gubernamentales, la intención es ayudar a los estados miembros a encontrar soluciones.

Si usted está interesado en participar en la reunión técnica o tiene un proyecto que puede ser considerado, sírvase enviar su nombre, dirección, así como una breve descripción del proyecto antes del 1 de agosto de 1999 a:

IPGH HQ
Comisión de Cartografía
Ciudad de Mexico,
Ex- Arzobispado 29,
Col. Observatorio, 11860
Mexico, D.F.

The Pan American Institute of Geography and History (PAIGH) Commission on Cartography Technical Meeting

The PAIGH Commission on Cartography has scheduled a technical meeting at the University of Panama, from Sept. 22 to 26, 1999 to discuss technical problems facing countries of Central and South America in the areas of Cartography, Remote Sensing, Geographic Information Systems and Geospatial Data. The goal of this meeting is to identify, with the participation of representatives from Central and South America PAIGH member states, technical projects that address issues of importance in these areas. The intention is for PAIGH and other non-governmental organizations to assist the member states in developing solutions. If you are interested in participating in the technical meeting or have a project for consideration please send your name, address and a short description of the project no later then August 1, 1999 to:

PAIGH HQ
Commission on Cartography
Mexico City,
Ex-Arzobispado 29,
Col. Observatorio, 11860
Mexico, D.F.